SIMULATION OF SEMICONDUCTOR DEVICES AND PROCESSES Vol. 4
Edited by W. Fichtner, D. Aemmer - Zurich (Switzerland) September 12-14, 1991 - Hartung-Gorre

Optical Generation in Semiconductor-Device Analysis — A General-Purpose Implementation —

G. Verzellesi, M. C. Vecchi, M. Zen† and *M. Rudan*

Dipartimento di Elettronica, Informatica e Sistemistica
Università di Bologna, viale Risorgimento 2, 40136 Bologna, Italy
Tel.: +39 (51) 644-3016, Fax: +39 (51) 644-3073

† IRST — Divisione Scienza dei Materiali, 38050 Povo (Trento), Italy

Abstract

The description of the optical-generation phenomena has been incorporated in the semiconductor-device analysis program HFIELDS. This has been achieved by introducing a number of optical windows and interleaved material layers through which a radiation with arbitrary spectrum, incidence angle, and polarization state enters the crystal, and by evaluating the corresponding generation rate at each node of the discretization grid. The code equipped with this new capability makes the description of realistic semiconductor optical sensors feasible.

1. Physical aspects

The system of (non linear) PDE's constituting the semiconductor-device model and incorporating the optical-generation effects is made of Poisson's equation

$$\mathrm{div}(\varepsilon\,\mathrm{grad}\varphi) = -\rho \tag{1.a}$$

and of the electron- and hole-continuity equations

$$\frac{\partial n}{\partial t} - \frac{1}{q}\mathrm{div}\mathbf{J}_n = G_n^{opt} - U\,, \qquad \frac{\partial p}{\partial t} + \frac{1}{q}\mathrm{div}\mathbf{J}_p = G_p^{opt} - U\,, \tag{1.b}$$

supplemented by the drift-diffusion expression for the electron and hole current densities

$$\mathbf{J}_n = -q\mu_n n\,\mathrm{grad}\varphi + qD_n\mathrm{grad}n\,, \qquad \mathbf{J}_p = -q\mu_p p\,\mathrm{grad}\varphi - qD_p\mathrm{grad}p \tag{2}$$

and by the expression for the charge density. Eq. (1.a) holds in the semiconductor and in the insulator domains with

$$\rho = q(p - n + N_D^+ - N_A^-)\,, \qquad \rho = q\,N_{ox}\,, \tag{3}$$

respectively. The remaining equations hold in the semiconductor domains only. The symbols in Eqs. (1–3) have the customary meaning of the semiconductor-device theory. Hence, only the form of the optical terms G_n^{opt}, G_p^{opt} will be discussed here in some detail.
The numerical solution of system (1–3) is carried out in HFIELDS by discretizing the equations on a two-dimensional, triangular grid [1]. This transforms the system of PDE's in a (non-linear) algebraic system whose unknowns are the values of φ, n, and p at the grid nodes. To

[0]M. C. Vecchi avails herself of fellowships provided by SGS-Thomson. This work was supported in part by the Italian National Council of Research under the "Progetto Finalizzato MADESS".

incorporate the optical-generation effects it is then necessary to evaluate G_n^{opt} , G_p^{opt} at each grid node belonging to the semiconductor. This is done in two steps: in the first one, the intensity and the direction of the e.m. wave which actually enters the semiconductor crystal are evaluated. This calculation accounts for the characteristics of the impinging radiation and for the geometrical structure and physical nature of the material layers interleaved between the radiation source and the crystal. In the second step, the carrier generation produced by radiation at each grid node is evaluated.

The material layers mentioned above are modeled using the following simplifying assumptions. A stack of $m-2$ layers of different materials is considered, separated by plane and parallel interfaces. The stack is placed between medium 1 (*initial medium*), in which the radiation source is located, and medium m (*final medium*), coinciding with a semiconductor zone (Fig. 1). Further, it is assumed that *i)* all the m media are optically linear, isotropic, and homogeneous, *ii)* the initial and final media have an infinite extension in the direction z normal to the interfaces, *iii)* the e.m. wave is described by a superposition of plane and monochromatic waves. Thanks to the above hypoteses, the refraction angle θ'_m in the final medium and the transmission coefficient $\mathcal{T}$ of the whole structure (i.e., the fraction of the e.m. intensity transmitted to the final medium) are easily calculated for each monochromatic component of the impinging radiation. Quantities θ'_m and $\mathcal{T}$ turn out to depend on the frequency, initial angle of incidence θ_1 , and polarization state of the impinging radiation, on the layers' thicknesses, and on the (typically complex) refraction indices of all the media involved, $n_{ck} = n_k\,(1+j\zeta_k)$, $k = 1,\ldots,m$. Their expressions are [2]

$$\cos\theta'_m = q n_m\,(\cos\delta - \zeta_m \sin\delta)/Q\,, \qquad \sin\theta'_m = n_1 \sin\theta_1/Q\,,$$

$$\mathcal{T} = a^2\,\mathcal{T}_{TM} + b^2\,\mathcal{T}_{TE}\,,$$

where

$$q\,\exp(j\delta) = \cos\theta_m = \sqrt{1-\sin^2\theta_m}\,, \qquad \sin\theta_m = n_1/n_{cm}\,\sin\theta_1\,,$$

and

$$Q^2 = n_1^2 \sin^2\theta_1 + q^2 n_m^2\,(\cos\delta - \zeta_m \sin\delta)^2\,.$$

In the expression for $\mathcal{T}$, coefficients a , b are functions of the polarization state, and $\mathcal{T}_{TM}$, $\mathcal{T}_{TE}$, are the transmission coefficients for the magnetic transverse and electric transverse waves. By way of example, the transmission coefficient $\mathcal{T}$ of an air-SiO_2-Si structure is plotted in Fig. 2 vs. the wavelength at four different oxide thicknesses. The above expressions allow one to express the photon flux at the semiconductor surface and for each monochromatic component as

$$\Phi_{0\nu} = \mathcal{T} I^{(i)}/(h\nu)\,,$$

where $I^{(i)}$, $\mathcal{T} I^{(i)}$ are the intensities of the incident and transmitted wave, respectively, and $h\nu$ is the photon energy. For frequencies falling in the visible range it is a reasonable approximation to consider the electron excitation from the valence to the conduction band as the dominant absorption mechanism. Hence, each photon absorption produces one electron-hole pair, and the expression of $G_n^{opt} = G_p^{opt} = G^{opt}$ holds for each monochromatic component and for the total radiation as well. Furthermore, for a non-degenerate semiconductor the effects of the non-uniform doping and free carriers can be neglected. In this case, the absorption coefficient of the semiconductor $\alpha(\nu, T_L)$ is independent of the position and equals the intrinsic one [3,4] (T_L is the lattice temperature).

The photon absorption in the semiconductor is finally expressed by means of a Poisson statistical distribution in which the mean penetration length is $L = 1/\alpha$. For each monochromatic

component the photon flux at a given depth ξ in the semiconductor along the propagation direction turns out to be

$$\Phi_\nu(\xi) = \Phi_{0\nu} \exp(-\alpha\xi).$$

Since each photon absorption produces one electron-hole pair, it is

$$G_\nu^{opt}(\xi)\,d\xi = -d\Phi_\nu(\xi),$$

whence

$$G_\nu^{opt}(\xi) = \alpha\Phi_{0\nu} \exp(-\alpha\xi). \tag{4}$$

The total optical generation rate $G^{opt}(\xi)$ is then found by adding up the monochromatic contributions (4).

2. Software implementation

Optical generation has been implemented in such a way as to allow the maximum geometrical and structural flexibility. To this purpose, it is worth mentioning that HFIELDS has the capability of managing up to ten different semiconductor zones for a given device, supplemented with the necessary interfaces with insulating zones and different types of contacts, gates, and floating gates. As for the illumination conditions, the code has been given the capability of managing up to ten illumination windows for each semiconductor zone. The illumination window is defined as the portion of the semiconductor boundary on which a radiation impinges. Consistently with the hypoteses outlined in the previous paragraph, each window is a segment laying along the boundary, hence it suffices for its definition to provide the coordinates of the two edges (they need not coinciding with any of the grid nodes). The additional parameters to be defined for each window are, first, the electromagnetic characteristics of the initial and final media, and the radiation incidence angle in the initial medium with respect to the window's normal. Then, the user may define up to six intermediate layers by providing the electromagnetic characteristics and thickness for each of them. As for the nature of the impinging radiation, up to nine monochromatic waves are definable for each window by providing the individual wavelength, intensity, and polarization state. As anticipated in the previous paragraph, the effects of the individual wavelengths on the total optical generation rate is found by adding up the monochromatic contributions. In addition to that, a further parameter allows for the definition of a black-body radiation, whose temperature is imposed by the user. For each window, the black-body radiation is partitioned in a suitable number of monochromatic components whose effects are then added to those of the individually-defined monochromatic waves.
Let us now focus on the evaluation of the generation rate at a specific node, say node i, in the semiconductor. For each window and monochromatic wave the number of photons and the final refraction angle θ'_m are determined. Then, a two dimensional strip is constructed by drawing two lines starting from the window's edges and entering the semiconductor in the θ'_m direction (Fig. 3). If node i falls within the strip, its distance ξ_i from the window is calculated and the contribution to the optical generation is determined according to (4). The procedure is then repeated in a double loop scanning the monochromatic components defined for each of the existing windows, and accumulating the result in the total generation rate $G^{opt}(\xi_i)$.

3. Results

The validity of the proposed model has been tested first on a specially-designed, CMOS-compatible photodiode fabricated at IRST. The structure under test (Fig. 4) consists of a

square photodiode (200×200 μm^2) made by a p^+ region diffused in an n-well region. Two guard rings provide the device isolation with respect to the carriers generated outside the photodiode area. The relatively large dimensions of the photodiode allow for an easier characterization of both physical and electro-optical parameters. The peak values of the doping concentrations are 5×10^{19} cm^{-3} and 1×10^{16} cm^{-3} in the p^+ and n-well region, respectively. In the p substrate the dopant concentration ranges from 4×10^{14} cm^{-3} to 4×10^{16} cm^{-3}. The oxide thickness is $t_{ox} = 3$ μm, whereas the junction depths are $x_{jp} = 0.7$ μm and $x_{jn} = 4.7$ μm for the p^+ and the n-well regions, respectively. Both the above regions are accessed through lateral contacts. The electro-optical measurement setup consists of a monocromator-illuminator system with a halogen lamp source and a reference calibrated detector. Orthogonally-impinging radiation at a wavelength ranging from 450 to 700 nm has been selected. An HP 4145B parameter analyzer has been used for the measurement of the electrical parameters.

Figs. 5 and 6 show the results of the numerical simulation and experiments, respectively. In these figures, the normalized current vs. reverse bias is reported at different wavelengths. Two different terms contribute to the photocurrent: the first one (diffusive) refers to the optical generation in the quasi-neutral regions of the diode, while the second (ohmic) is due to the optical generation in the depletion region. The results obtained show that for long wavelengths the photocurrent is dominated by the diffusive term, and depends weakly on the bias values because the optical generation occurs just beneath the semiconductor surface, i.e., far from the depletion region of the p^+n junction. Conversely, the ohmic term becomes more important for short wavelengths, reaching the depleted layer, and the photocurrent exhibits a stronger dependence on the applied bias.

The comparison between the experimental and simulation data shows a good agreement for wavelengths larger that 550 nm, while at shorter wavelengths the agreement becomes poorer. This is ascribed to the fact that the shorter wavelength response is affected by several surface effects (e.g., the presence of surface charges, which have not been taken into account in the model).

In Fig. 7 the simulated and experimental photodiode spectral response vs. wavelength, at constant impinging power density (90 $\mu W/cm^2$) and constant reverse bias (1 V), are shown. The experimental spectrum has been normalized to the lamp spectral response. The photodiode spectral response shows several peaks due to the multiple reflection and interference phenomena resulting from the presence of a stack of SiO_2 layers above the semiconductor surface. Preliminary simulations showed that the number and position of the peaks depends more critically on the stack's total thickness than on the thickness and composition of the individual layers, since the latters present similar values of the refraction index. Therefore, in the final simulation an uniform 3.0 μm SiO_2 has been used. At shorter wavelengths the reduced experimental responsivity with respect to the simulation data is evident, and is to be ascribed to the surface effects mentioned above. In the central part of the spectrum the qualitative and quantitative agreement is rather satisfactory.

A second set of simulations has been carried out on a similar device whose size, oxide thickness, and doping distribution have been selected in order to reproduce the experimental device presented in [4]. More specifically (referring again to the structure of Fig. 4), the oxide thickness is 0.2 μm, the p substrate has a constant acceptor concentration $N_{sub} = 5 \times 10^{15}$ cm^{-3}, the n-well region is made of an epitaxial layer with $N_{epi} = 7 \times 10^{14}$ cm^{-3} and $x_{jn} = 7.56$ μm, and the p^+ region is made of a diffusion whose peak concentration is 5×10^{18} cm^{-3}. The standard deviation of the diffusion is selected in order to have $x_{jp} = 0.56$ μm, so that $x_{jn} - x_{jp} = 7$ μm. As described in [4], this structure is a part of a more complex circuit used for color sensing.

Its bias values are selected as follows: both junctions are reversely biased and, given the bias V_L of the lower junction, the upper one V_U is tuned in such a way as to deplete the n-well region completely. In this way, for each pair (V_U, V_L) the inversion point of the electric field will occur at a different position in the n-well region. By way of example, the electric potential along a device section obtained by HFIELDS at $V_U = 8$ V is shown in Fig. 8. The position of the inversion point of the electric field is about $x_{inv} = 4.35$ μm in this case. At a given value of x_{inv}, the upper contact will collect only the holes generated in the region $x \leq x_{inv}$. In particular, for a monochromatic radiation at frequency ν the amount of collected holes will depend on the relative magnitude of $L = 1/\alpha(\nu)$ and x_{inv}, thus providing a correlation between current and frequency.
The results of the simulations carried out on the device described above are shown in Figs. 9, 10. In the first one the current due to the optically generated holes collected at the upper contact is drawn as a function of V_U at different wavelengths. The current is normalized to its value at $V_U = 15$ V which, for the frequency range under investigation, corresponds to a position of the inversion point deep enough in the n-well region to have the majority of holes collected by the upper contact. In Fig. 10 the simulated and experimental relative spectral response η (defined as $\eta = I_U/qAT\Phi_{0\nu}$, where I_U represents the current at the upper contact and A is the junction area) vs. wavelength, at constant reverse bias $V_U = 1$ V, are shown. In both Figs. 9 and 10, the dots are the experiments taken from [4], the continuous lines are the simulations. Despite the surface effects (taken into account in [4] but not in the simulation), which make the agreement poorer at shorter wavelengths, the agreement is satisfactory.

4. Conclusions

The examples of the previous paragraph show that the introduction of the optical-generation effect in a semiconductor-device analysis program as HFIELDS allows for a detailed characterization of the photogenerated current with respect to the standard analytical approach. The effect of the multiple reflection and interference phenomena exhibited by the spectral response of the sensor cleary justifies the computational effort required by the evaluation of the e.m. wave propagation through the material layers. This becomes particularly relevant for the many applications where the dependence of the solid-state sensor response on the wavelength of the impinging radiation is critical.

References

[1] G. Baccarani, R. Guerrieri, P. Ciampolini, M. Rudan, HFIELDS: a *Highly Flexible* 2-D *Semiconductor-Device Analysis Program*, Proc. of the NASECODE IV Conference, Dublin: J. J. H. Miller Ed., pp. 3–12, 1985

[2] M. Born, E. Wolf, *Principles of Optics*, Pergamon Press, 1980

[3] H. R. Philipp, E. A. Taft, *Optical Constants of Silicon in the Region 1 to 10 eV*, Physical Review, Vol. 120, No. 1, 1960

[4] R. Wolfenbuttel, *Integrated Silicon Colour Sensors*, Delft University of Technology, 1988

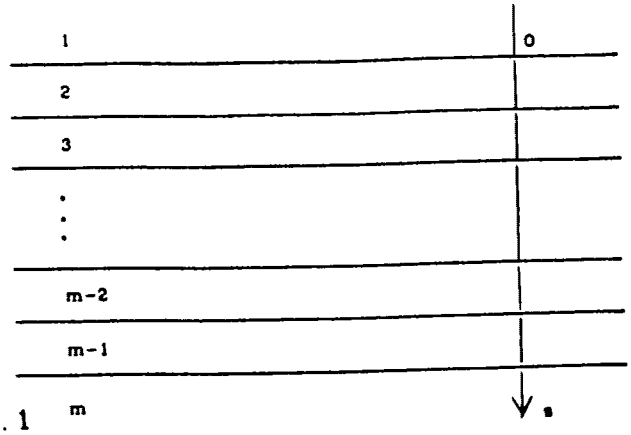

Fig. 1

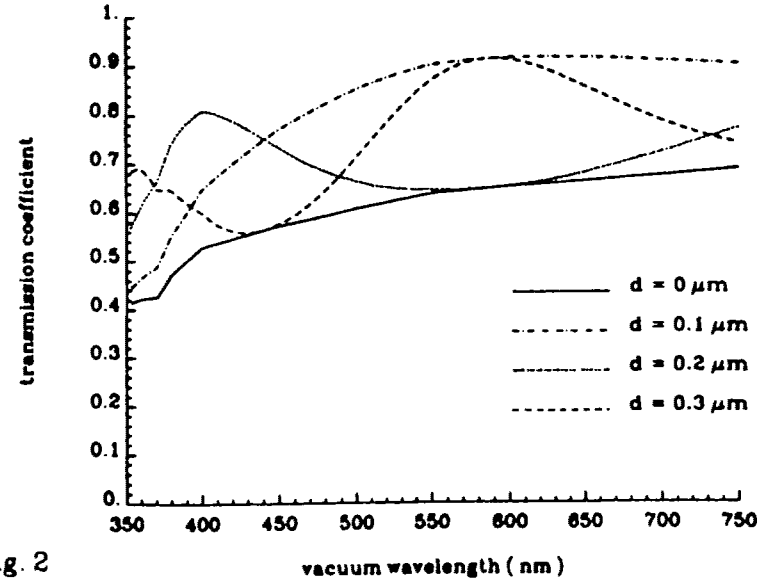

Fig. 2

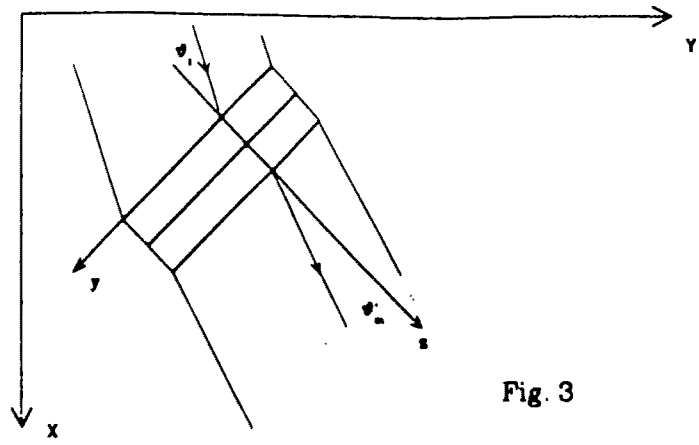

Fig. 3

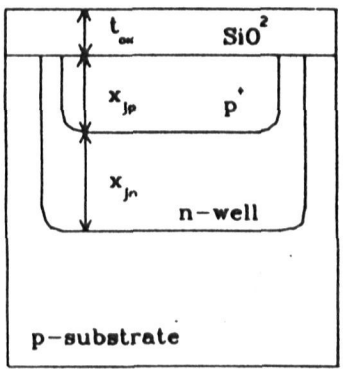

Fig. 4

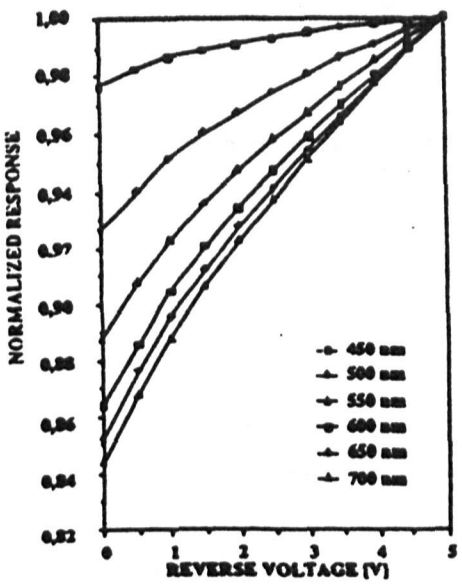

Fig. 5

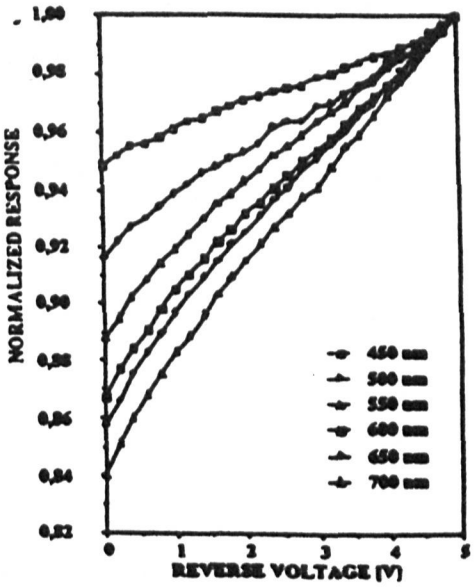

Fig. 6

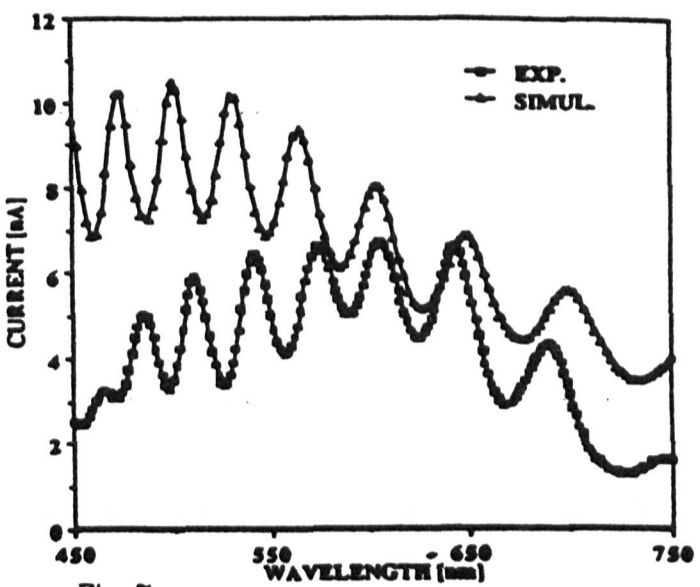

Fig. 7

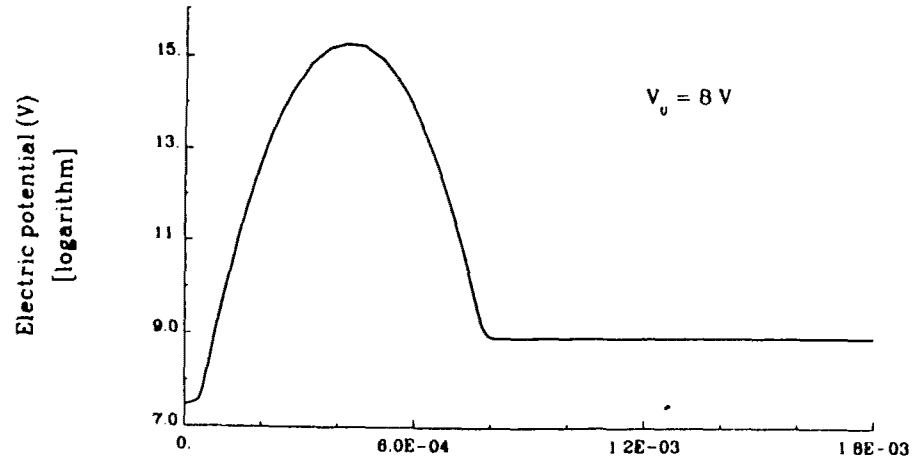

Fig. 8

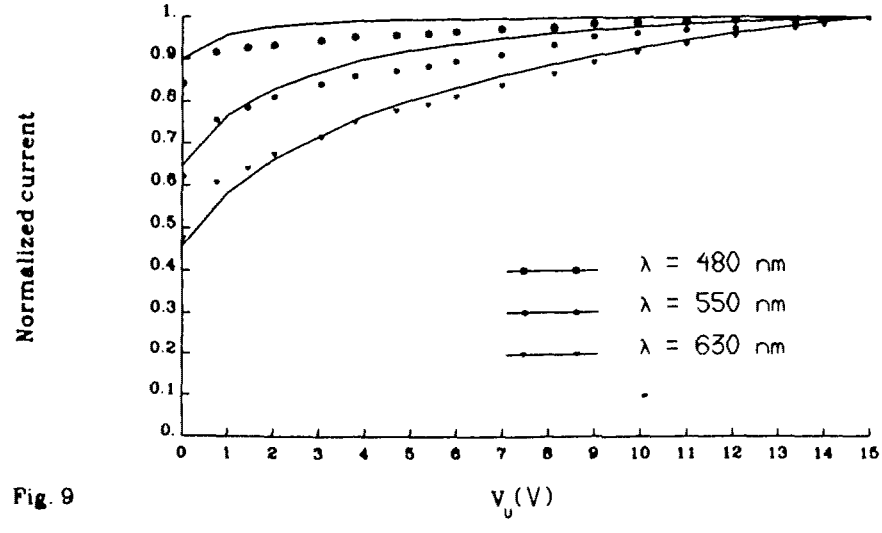

Fig. 9

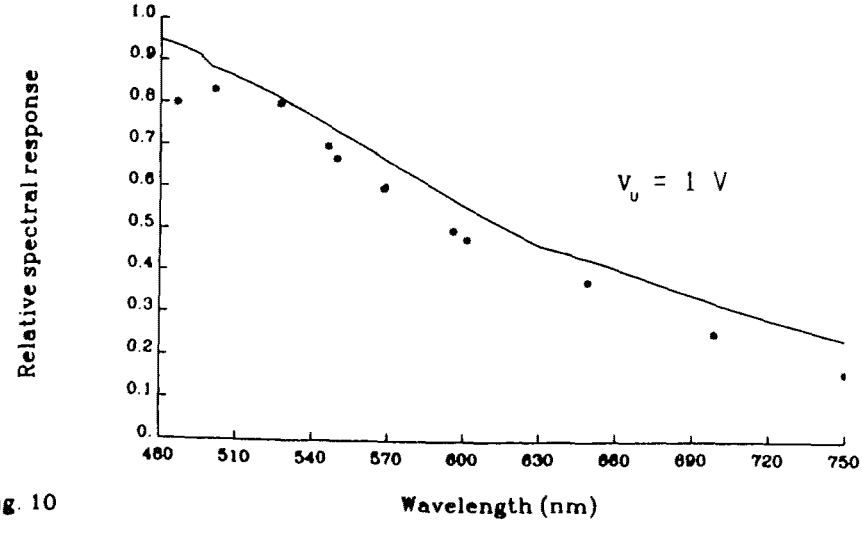

Fig. 10